International Forum on Aeroelasticity and Structural Dynamics
IFASD 2017
25-28 June 2017 Como, Italy

AEROELASTIC ANALYSIS OF A FLUTTER DEMONSTRATOR WITH A VERY FLEXIBLE HIGH-ASPECT-RATIO SWEPT WING

Vladyslav Rozov[1], Andreas Hermanutz[2], Christian Breitsamter[1], Mirko Hornung[2]

[1]Technical University of Munich
Faculty of Mechanical Engineering
Chair of Aerodynamics and Fluid Mechanics
Boltzmannstr. 15, 85748 Garching, Germany
vladyslav.rozov@aer.mw.tum.de
christian.breitsamter@aer.mw.tum.de

[2]Technical University of Munich
Faculty of Mechanical Engineering
Chair of Lightweight Structures
Boltzmannstr. 15, 85748 Garching, Germany
andreas.hermanutz@tum.de
mirko.hornung@tum.de

Keywords: flutter, small-disturbance CFD, structural dynamics, aeroelasticity, flexible wing

Abstract: The goal to develop aircraft which are greener, safer, and more cost effective can be only maintained by significant innovations in aircraft design methods. An integrated multidisciplinary design approach can lead to a considerable performance enhancement of future derivative aircraft. Advanced aerodynamic and structural design technologies can be achieved by passive as well as active suppression of aeroelastic instabilities. To demonstrate the potential of this approach, an UAV with a high-aspect-ratio wing and clearly predefined flutter characteristics is developed within the EU funded project *Flutter Free FLight Envelope eXpansion for ecOnomical Performance improvement* (FLEXOP). The FLEXOP UAV will be used as an experimental test platform. The aeroelastic behavior of the preliminary aircraft design is investigated. Therefore, a tool for aeroelastic analysis based on a small-disturbance Euler solver is deployed. The results obtained by means of the small-disturbance Euler solver and a doublet lattice method (DLM) based on linear potential theory are compared and discussed.

1 INTRODUCTION

The success of aircraft manufacturers depends on continuous improvement of efficiency and reduction of the operating costs of aircraft. In the near future, these tasks will be mainly achieved by derived aircraft designs. On the one hand, this approach ensures the development costs to be kept low. On the other hand, this approach allows only for a limited scope of improvements. Such modifications include stretching of the fuselage, more efficient engines, etc. This methodology allows only a small increase in efficiency over the previous aircraft generation compared to a completely new design.

The potential of this strategy can be augmented by an integrated design approach (IDA). Thereby, aeroelastic and flight control considerations are integrated at early stages in the design process.

This leads to an enhancement of the aircraft performance and a reduction of development and certification costs. Moreover, IDA can help to circumvent existing limitations in the development of derived aircraft by expanding the design space. A promising field of its application is the flexible wing technology. Thereby, the main goal is to increase the efficiency of an existing wing at no excess of its structural weight, whereas the flight envelope is preserved or even extended. The task can be mainly accomplished by increasing the span (and thus aspect ratio) of the wing. The aeroelastic challenges that arise alongside are addressed by means of aeroelastic tailoring and active control.

To demonstrate the potential of IDA, an affordable experimental test platform with a high-aspect-ratio wing design is developed within the project FLEXOP. New multidisciplinary methods and tools for aeroelastic tailoring and active control are developed and validated on three different wing configurations with clearly predefined structural and aeroelastic characteristics. Active flutter control methodologies will be tested on the flutter wing. To ensure an affordable realization it has been designed to feature a low flutter velocity as well as frequency. Because of strict design margins, methods for an accurate flutter prediction become particularly essential throughout the entire development process. To gain a confidence in flutter boundaries it is desirable to perform a flutter analysis by means of different techniques for aerodynamic modeling. In this paper a flutter analysis of the FLEXOP demonstrator UAV equipped with the flutter wing is presented. The study is carried out employing the DLM as well as high-fidelity unsteady CFD method based on the small-disturbance (SD) approach.

2 THEORY AND NUMERICAL METHODS

In the following, the CFD-based methodology used for the aeroelastic analysis within this work is outlined.

2.1 Equations of aeroelasticity

The starting point for a CFD-based aeroelastic analysis is a system of equations describing the motion of a general structural system under the influence of external forces $\boldsymbol{f}(t)$. These equations are typically formulated in terms of physical coordinates, i.e. displacements and rotations. It is convenient to reduce the order of the system by transferring it into generalized coordinates. Thus, the equations of motion can be written as

$$\begin{aligned} \boldsymbol{M}_{gen}\ddot{\boldsymbol{q}}(t) + \boldsymbol{C}_{gen}\dot{\boldsymbol{q}}(t) + \boldsymbol{K}_{gen}\boldsymbol{q}(t) &= q_\infty l_{ref}^3 \cdot \boldsymbol{f}_{gen}(t) \\ \text{with} \quad \boldsymbol{f}_{gen}(t) &= \boldsymbol{\Phi}^T \boldsymbol{f}(t) \end{aligned} \tag{1}$$

Thereby, $\boldsymbol{\Phi} = [\boldsymbol{\phi}_1, \boldsymbol{\phi}_2, \ldots, \boldsymbol{\phi}_N]$ is the modal matrix, which comprises N mode shapes $\boldsymbol{\phi_i}$. It can be interpreted as a linear operator, which describes the transformation between the physical and generalized coordinates:

$$\boldsymbol{x}(t) = \boldsymbol{\Phi}\boldsymbol{q}(t) \tag{2}$$

The matrices $\boldsymbol{M}_{gen}, \boldsymbol{C}_{gen}$, and $\boldsymbol{K}_{gen}$ are diagonal and contain generalized mass, damping, and stiffness for each modal coordinate. The vector $\boldsymbol{f}_{gen}(t)$ denotes the generalized aerodynamic forces, which are obtained within this study as a result of a CFD simulation. The dynamic pressure q_∞ and the cube of the grid reference length l_{ref}^3 arise in Eq. 1 due to a nondimensional formulation of the CFD code. Each element of the vector $\boldsymbol{f}_{gen}(t)$ can be computed for pressure-induced aerodynamic forces as follows:

$$f_{gen,i}(t) = \int_{\boldsymbol{S}} c_p[\boldsymbol{\phi}_i] \cdot \mathrm{d}\boldsymbol{S} \tag{3}$$

The vector $[\boldsymbol{\phi}_i]$ represents a chunk of $\boldsymbol{\phi}_i$ describing the mode shape deflection at a point of the surface $\boldsymbol{S}$. It can be seen, that the contribution of the pressure-induced load $c_p = (p - p_\infty/q_\infty)$ to generalized aerodynamic force scales with the scalar product of the mode shape deflection $[\boldsymbol{\phi}_i]$ and the surface normal vector $\mathrm{d}\boldsymbol{S}$.

With respect to the major assumptions concerning a classical aeroelastic stability analysis, sufficiently small structural deflections are considered throughout this work. Hence, the relation between structural deflections and thereby encountered unsteady aerodynamic forces is linear. Therefore, the principle of superposition can be used to describe the aerodynamic response to a transient structural excitation [1]. Employing the impulse response matrix $\boldsymbol{Q}(t)$ formulated in terms of generalized coordinates, the generalized aerodynamic forces can be computed by means of the convolution integral:

$$\boldsymbol{f}_{gen} = \int_{\tau=0}^{t} \boldsymbol{Q}\left(t-\tau\right) \cdot \boldsymbol{q}\left(\tau\right) \mathrm{d}\tau \tag{4}$$

However, the frequency domain formulation of Eq. 1 is used within this work. It is the well-established flutter equation, which can be written as:

$$\left[-\omega^2 \boldsymbol{M}_{gen} + i\omega \boldsymbol{C}_{gen} + \boldsymbol{K}_{gen} - q_\infty l_{ref}^3 \cdot \boldsymbol{GAF}\left(ik_{red}\right)\right] \cdot \boldsymbol{q}_0 = \boldsymbol{0} \tag{5}$$

In this context, ω denotes the angular velocity. k_{red} is a dimensionless frequency parameter usually defined in terms of the semi-chord $MAC/2$ and freestream velocity V_∞:

$$k_{red} = \frac{\omega \cdot MAC}{2V_\infty} \tag{6}$$

$\boldsymbol{GAF}$ is the transfer matrix. Each term GAF_{ij} is a complex quantity representing the magnitude and phase of the force $f_{gen,i}$ acting on the generalized coordinate i due to a harmonic motion of the generalized coordinate j with a unit amplitude at a frequency k_{red}.

2.2 Nonlinear and small-disturbance-based CFD solver

A small-disturbance (SD) Euler solver AER-SDEu, developed by Kreiselmaier and Laschka [2] at the Chair of Aerodynamics and Fluid Mechanics of the Technical University of Munich is used for computation of the generalized aerodynamic forces. The SD approach, compared to established linear potential methods, provides a better accuracy with regard to complex three-dimensional flows. Additionally, it is able to capture transonic flow phenomena such as shocks. SD-based aerodynamic modeling has been successfully applied for a range of applied problems with regard to unsteady aerodynamics [3–9]. The SD-Euler solver is based on the nonlinear Euler solver AER-Eu. AER-Eu uses the Finite-Volume (FV) method for the discretization of the Euler equations formulated in terms of curvilinear coordinates ξ, η, ζ:

$$\frac{\partial \boldsymbol{Q}}{\partial \tau} + \frac{\partial \boldsymbol{F}}{\partial \xi} + \frac{\partial \boldsymbol{G}}{\partial \eta} + \frac{\partial \boldsymbol{H}}{\partial \zeta} = \boldsymbol{0} \tag{7}$$

Thereby, the equations describe the conservation of mass, momentum, and energy. The conservative variables build up the vector $\boldsymbol{Q}$. $\boldsymbol{F}$, $\boldsymbol{G}$, and $\boldsymbol{H}$ define convective fluxes of $\boldsymbol{Q}$ in ξ-, η-, ζ-direction.

The numerical fluxes are calculated by Roe's flux difference splitting [10]. The underlying reconstruction of the conservative variables at FV-cell faces is performed by the MUSCL scheme [11]. Hence, it leads to the second-order accuracy in space and guarantees the total-variation-deminishing property. The steady-state solution process is carried out with a pseudo-time marching. Thereby the lower-upper-symmetric successive overrelaxation (LU-SSOR) scheme for the integration in pseudo-time is used [12]. The Small Disturbance method is derived from the nonlinear equations and adresses unsteady fluid dynamics problems. A small harmonic oscillation of the flow variables around a reference flow state is assumed. Given a flow variable χ, it can be defined as:

$$\boldsymbol{\chi}(\xi,\eta,\zeta,\tau) = \bar{\boldsymbol{\chi}}(\xi,\eta,\zeta) + \hat{\boldsymbol{\chi}}(\xi,\eta,\zeta)\cdot e^{ik\tau} \tag{8}$$

Additionally, if the flow is effected by a geometrical perturbation, oscillations of variables γ defining the geometrical metric of the computational grid have to be taken into account:

$$\boldsymbol{\gamma}(\xi,\eta,\zeta,\tau) = \bar{\boldsymbol{\gamma}}(\xi,\eta,\zeta) + \hat{\boldsymbol{\gamma}}(\xi,\eta,\zeta)\cdot e^{ik\tau} \tag{9}$$

Bars over variables denote the reference state, whereas hats indicate complex valued disturbance parts of the variables. Due to the small disturbance assumption a linearization process of the unsteady Euler equations (Eq. 7) around the reference state is justified. Thus, an unsteady problem can be reduced to a steady-state problem. It can be shown, that inserting Eq. 8 and 9 into Eq. 7 yields the following system of equations:

$$\frac{\partial\hat{\boldsymbol{Q}}^{(1)}}{\partial\tau} + \frac{\partial\hat{\boldsymbol{F}}^{(1)}}{\partial\xi} + \frac{\partial\hat{\boldsymbol{G}}^{(1)}}{\partial\eta} + \frac{\partial\hat{\boldsymbol{H}}^{(1)}}{\partial\zeta} = - \left(\hat{\boldsymbol{Q}}^{(1)}\cdot ik + \hat{\boldsymbol{Q}}^{(2)}\cdot ik + \frac{\partial\hat{\boldsymbol{F}}^{(2)}}{\partial\xi} + \frac{\partial\hat{\boldsymbol{G}}^{(2)}}{\partial\eta} + \frac{\partial\hat{\boldsymbol{H}}^{(2)}}{\partial\zeta} \right) \tag{10}$$

The resulting system of equations has to be solved for the disturbance parts of the flow variables. Terms which depend on disturbance parts of flow variables and the reference grid metric are denoted by a superscript $^{(1)}$. The terms marked by the superscript $^{(2)}$ depend on the reference flow state and the disturbance parts of the geometrical metric. $^{(2)}$-terms act as a source. They are known and can be computed prior to the solution process. A steady-state solution of the AER-Eu serves as an input for the reference flow state.

Once a SD-solution is computed for a certain reduced frequency k_{red}, unsteady aerodynamic loads harmonically acting with k_{red} upon the structure are known. Subsequently, $\boldsymbol{GAF}$ can be evaluated directly as follows for an entry GAF_{ij}:

$$GAF_{ij} = \int_{\boldsymbol{S}} \hat{c}_{p,j}\left[\bar{\boldsymbol{\phi}}_i\right]\cdot\overline{\mathrm{d}\boldsymbol{S}}_j + \int_{\boldsymbol{S}} \bar{c}_{p,j}\left[\hat{\boldsymbol{\phi}}_i\right]\cdot\widehat{\mathrm{d}\boldsymbol{S}}_j \tag{11}$$

3 FLEXOP DEMONSTRATOR UAV

3.1 Aircraft configuration

The FLEXOP demonstrator is designed such that its aeroelastic behavior is as close as possible to that of a commercial aircraft. The total takeoff weight of the aircraft including all its components and fuel is 59 kg. The wing with a leading edge sweep of $20°$ has a high aspect ratio of 19.7, a span of 7.07 m and an area of 2.54 m^2. The mean aerodynamic chord (MAC) is 0.37 m. The length of the fuselage is 3.44 m. The planform geometry of the FLEXOP UAV is depicted in Fig. 1.

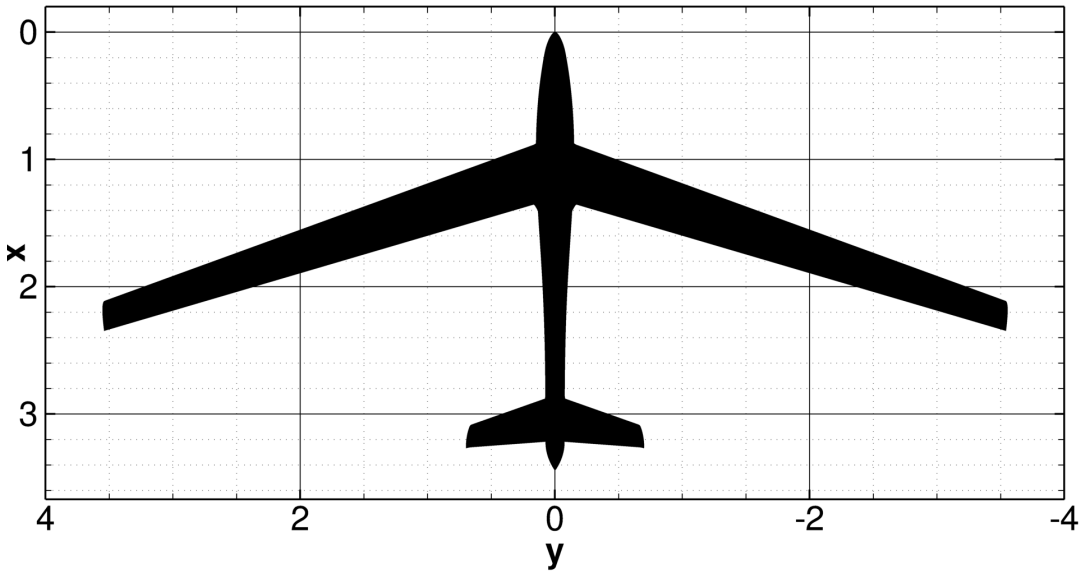

Figure 1: FLEXOP UAV planform geometry.

The tail control surfaces are arranged in a V-tail configuration. The thrust is generated by a jet engine mounted on top of the fuselage behind the wing trailing edge. The influence of the engine on the aircraft aerodynamics is neglected within this study.

3.2 Finite element model

A structural as well as an aerodynamic model is set up by means of MSC.Nastran [13]. The structure is modeled by means of the Finite Element (FE) method. Due to very limited design margins, an accurate structural modeling was preferred. Therefore, the FE model exhibits a high degree of detail. The components are represented as beam, shell, or solid elements depending on their structural loading. The overall model consists of approximately $1.6 \cdot 10^6$ elements. Modeling the components as individual parts allows reducing the errors caused by the offsets of the shell formulation. This approach is important to ensure a correct representation of the UAV's structure. The FE model of the FLEXOP demonstrator UAV is depicted in Fig. 2.

The aerodynamic model within MSC.Nastran is based upon a FE approach [13]. Aerodynamic elements are formulated in terms of the DLM, which is derived from the linearized aerodynamic potential theory [14,15]. Fig. 3 illustrates a strategy to connect the aerodynamic to the structural model. Here, a junction between the fuselage and the wing is shown. On the one hand, mapping nodes (white) relate aerodynamic and structural grid point deflections. On the other hand, they transfer aerodynamic forces to structural grid points. Aerodynamic load is distributed due to

rigid body elements RBE3. Rigid body elements RBE2 (blue) connect mapping nodes and, thus, define their relative motion. The aerodynamic element grid as well as RBE2-distribution over the wing is depicted in Fig. 4.

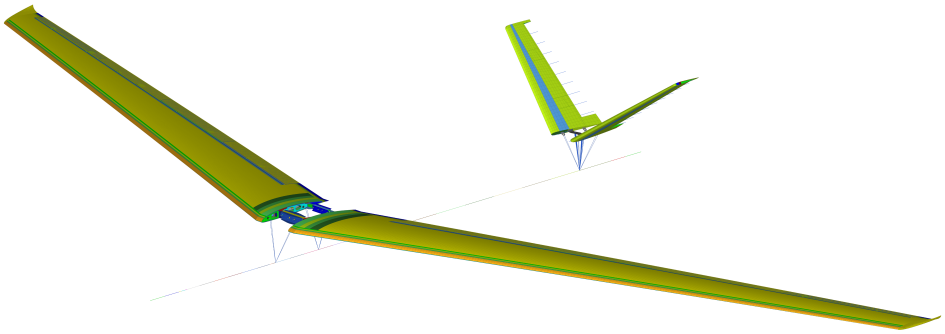

Figure 2: FE model of the FLEXOP demostrator UAV.

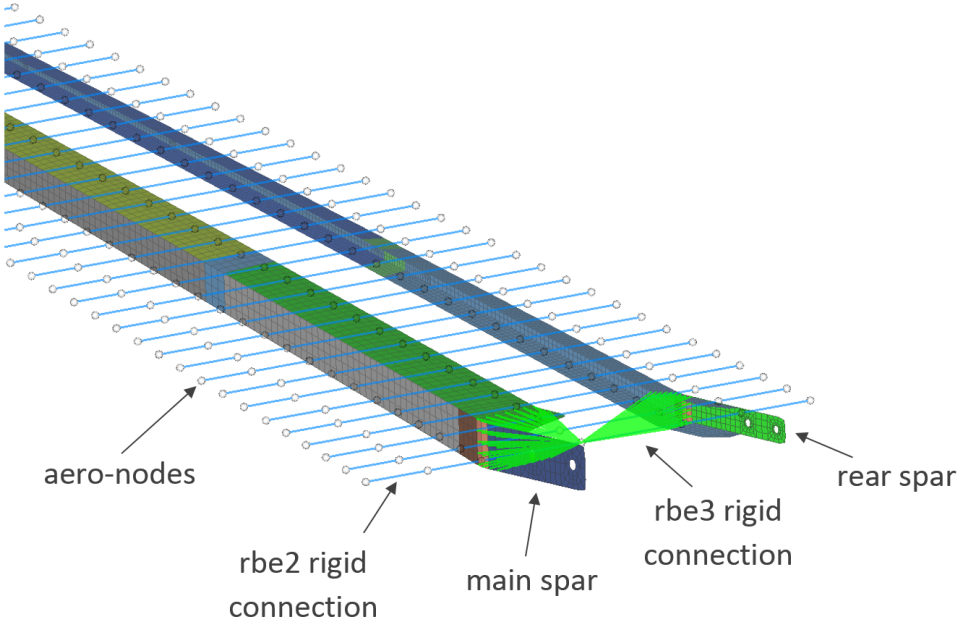

Figure 3: Interface between aerodynamic and structural model.

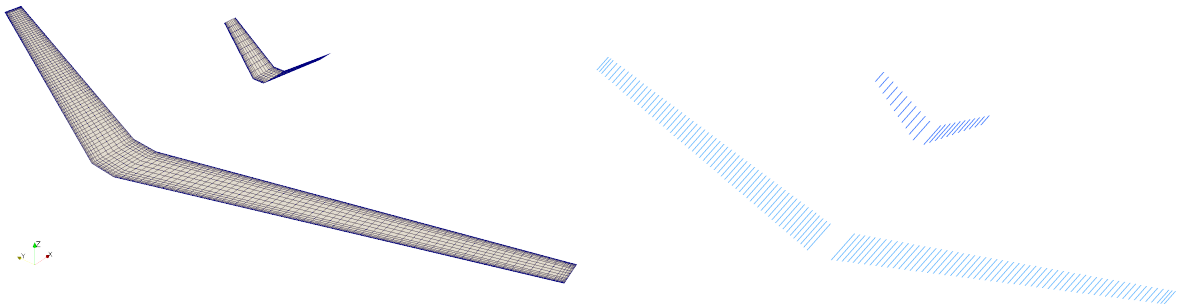

(a) Aerodynamic element grid (b) RBE2-distribution

Figure 4: Aerodynamic MSC.Nastran model.

3.3 Computational Grid

The structured grid used in this study was generated using ICEM CFD HEXA. The computational domain is descretized by $8.6 \cdot 10^6$ hexahedral elements. A multi-block topology approach was used. The chosen blocking strategy allows to easily include the engine geometry for future aerodynamic as well as aeroelastic investigations. The distance to the far-field in x-direction is set to 15 and 14 semi-spans upstream and downstream of the aircraft, respectively. The far-field in y- and z-directions is chosen to be at a distance of 15 semi-spans. The first grid-line is placed at a normal distance of 0.1 mm from the wall. It is approximately $3 \cdot 10^{-4} \cdot MAC$. The wing geometry is discretized with 83 FV-cells chordwise and 208 FV-cells spanwise. The surface grid of the FLEXOP UAV is shown in Fig. 5.

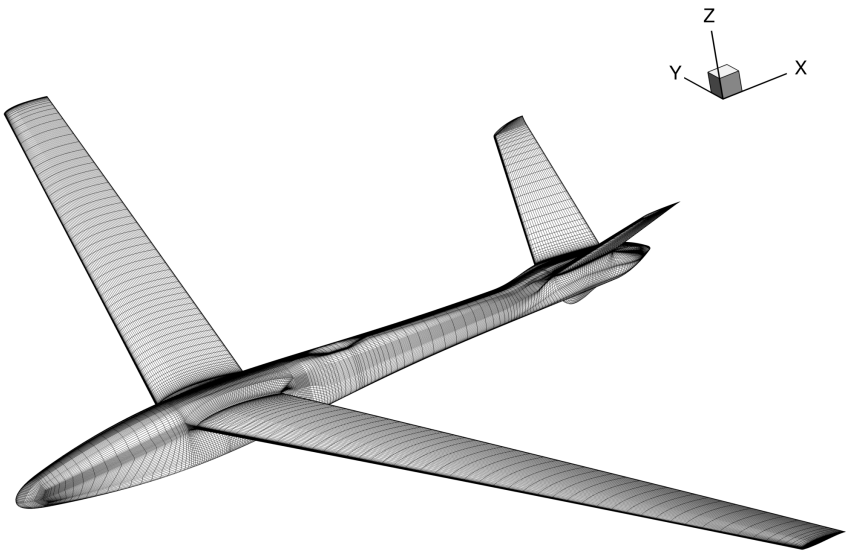

Figure 5: Surface grid of the FLEXOP UAV.

Perturbed grids are required as an input for the computation of the $^{(2)}$-terms. Therefore, the original surface CFD grid is deformed with respect to the shape of each structural mode based on the thin-plate spline interpolation [16]. Subsequently, the outer region of the computational domain is adjusted according to the surface grid deflection. This task is accomplished by means of the transfinite interpolation [17]. Mode shapes are rescaled such that the maximum deflection does not exceed 4 mm or approximately $1\% MAC$.

4 RESULTS

In this section, results of the modal analysis as well as the aeroelastic analysis conducted by means of the DLM as well as the small-disturbance Euler solver are presented.

The FE model was analyzed to provide the structural eigenmodes and natural frequencies for the FLEXOP demonstrator UAV. The eigenmodes are used as generalized coordinates q_i in the context of the SD-based aeroelastic analysis. Within this preliminary study the fuselage is fixed, thus only elastic eigenmodes of the structure are taken into consideration. External flutter tuning masses, mounted aft of the wing tip reduce the natural frequencies of the torsion dominated eigenmodes and, thus, the flutter velocity and frequency. The V-tail structure is very stiff in

contrast to the structure of the wing. Therefore, eigenmodes involving elastic deformation of the V-tail occur at higher frequencies starting at 40 Hz. Hence, the first eight eigenmodes, which are taken into consideration within the study, solely involve the wing deformation. They are plotted in Fig. 6 by means of the displacement magnitude.

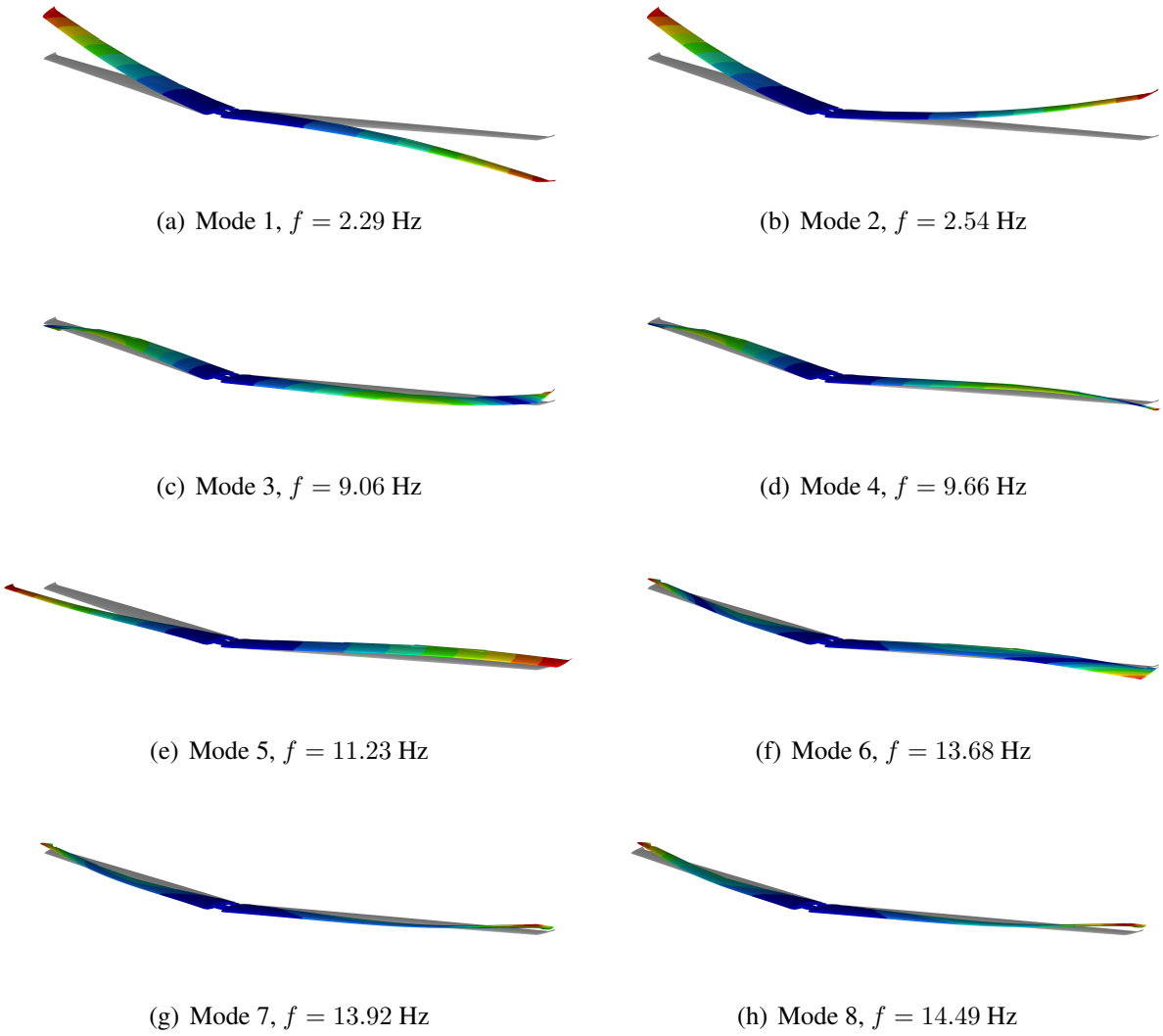

(a) Mode 1, $f = 2.29$ Hz

(b) Mode 2, $f = 2.54$ Hz

(c) Mode 3, $f = 9.06$ Hz

(d) Mode 4, $f = 9.66$ Hz

(e) Mode 5, $f = 11.23$ Hz

(f) Mode 6, $f = 13.68$ Hz

(g) Mode 7, $f = 13.92$ Hz

(h) Mode 8, $f = 14.49$ Hz

Figure 6: First eight structural eigenmodes. f denotes the natural frequencies of the modes.

The aeroelastic study is carried out for flight conditions corresponding to the envisaged flutter flight test. The load factor is $1g$ and the Mach number is set to $Ma_\infty = 0.15$. The density is 1.13365 kg/m^3, which corresponds to an altitude of 800 m above MSL according to the International Standard Atmosphere. Trim calculations, previously performed by MSC.Nastran, yielded a trim condition at an angle of incidence $\alpha = -0.2°$. This value ist used throughout all simulations. Moreover, for this preliminary study the aircraft is taken to be rigid. Thus, deformations due to static aeroelasticity at $1g$-flight are neglected.

The result of the steady-state AER-Eu-simulation at the previously described freestream conditions is used as a reference state for the SD simulations. Steady aerodynamic loads are visualized by means of the pressure coefficient contour plot in Fig. 7.

Unsteady aerodynamics at reduced frequencies $k_{red} = [0.0, 0.1, 0.2, 0.3, 0.5, 1.0, 3.0, 5.0]$ is used for the flutter analysis based on the DLM as well as the small-disturbance Euler simu-

lations. In the case of the SD-based approach, generalized aerodynamic forces are computed according to Eq. 11. Subsequently, the flutter equation (Eq. 5) is solved by means of the well-establisched p-k method [18]. Note also that the structural damping is set to zero.

The results of the flutter analysis for a velocity range from 5 to 70 m/s are presented in Fig. 8. The results based on the two approaches show good agreement. However, the damping behavior differs slightly between DLM- and SD-based results. The damping of the modes 1 and 2 increases with the velocity, whereas around 50 m/s the damping gradients become steeper. Here, in comparison to the DLM, the SD-based modeling predicts the gradients to be slightly shallower for both velocity regions, namely below and above 50 m/s. As velocity rises, the $6th$ as well as the $7th$ damping ratio increases linearly with a slope being higher for DLM- than SD-based aerodynamics. Moreover, according to both methodologies, the damping of the modes 5 and 8 remains at zero throughout the entire velocity range.

Slight differences are observed with regard to the frequency trends at higher velocity. Compared to DLM, SD-based aerodynamic modeling predicts higher increase in frequency for modes 6 and 7 on the one hand and lower decrease in frequency for modes 1 and 2 on the other hand.

According to the frequency trend, both methods predict the frequencies of the modes 3 and 4 to converge. Initially, the $3th$ and the $4th$ damping ratios increase, but wheres the velocity continues to increase, the damping starts to decrease around 30 m/s for both modes. Eventually, the modes become undamped. In comparison to the SD-based approach, the DLM yields a stronger damping for modes 3 and 4 in the stable velocity region. The quantitative difference in damping ratios leads to a slight change of the predicted stability boundaries. Within SD-based aerodynamic modeling, damping ratios 3 and 4 become zero at 43.64 m/s and 45.04 m/s respectively. DLM-based aerodynamic modeling predicts the stability boundaries for both modes to occur almost at the same velocity, namely at 49.58 m/s for mode 4 and at 49.6 m/s for

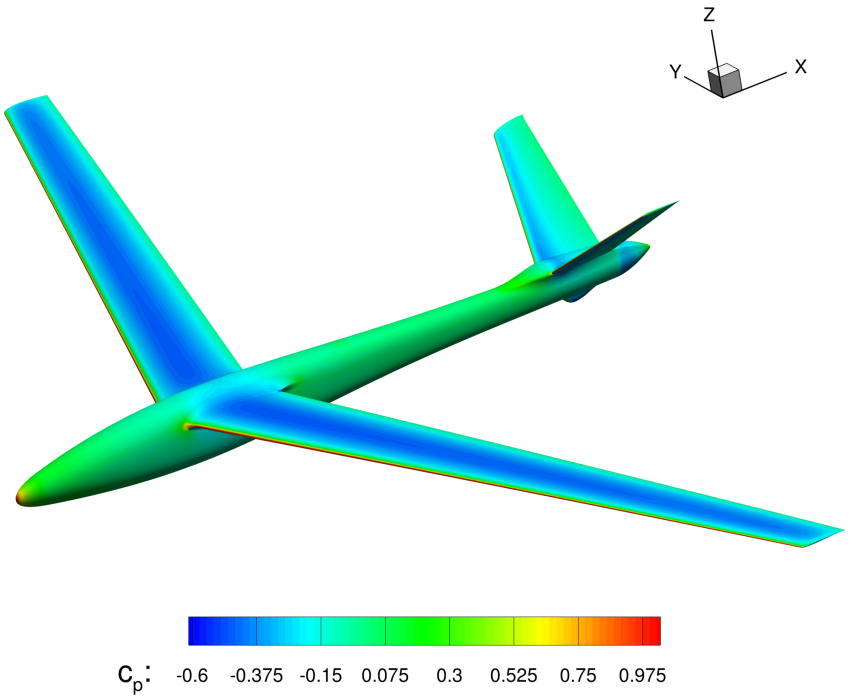

Figure 7: Contour plot of the c_p distribution at $Ma_\infty = 0.15$ and $\alpha = -0.2°$.

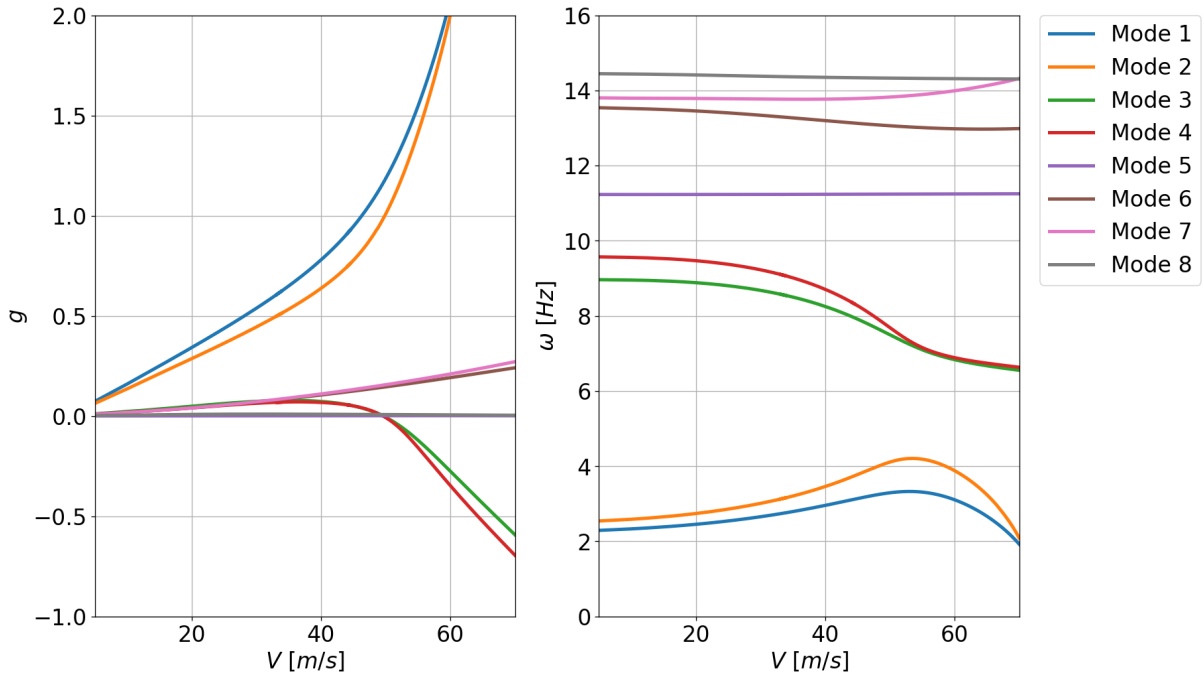

(a) DLM-based results

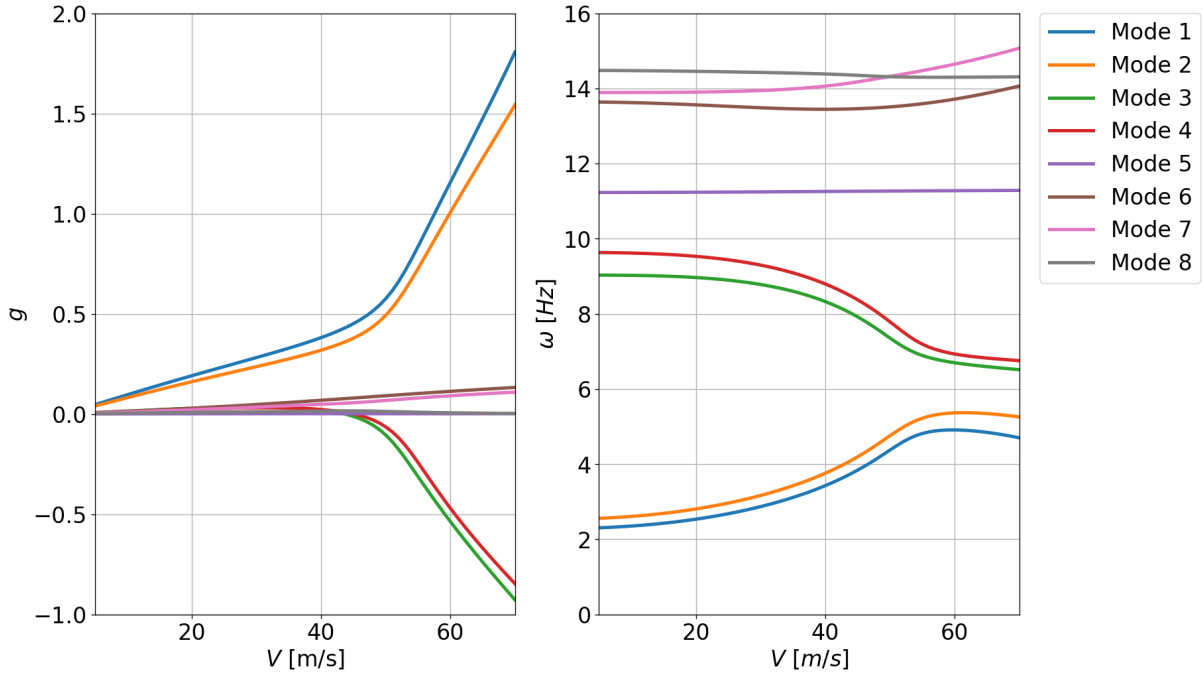

(b) SD-based results

Figure 8: Damping and frequency trends obtained by the p-k method for the DLM- as well as the SD-based approach

mode 3. Here, the mode 4 becomes unstable first, in contrast to the result obtained by the SD approach. An overview over stability boundaries along with frequencies at the boundary points predicted by both methods is provided in Table 1.

It can be seen, that both flutter modes show a similar behavior with respect to their damping and frequency trends, which can be explained by a similar mechanism leading to flutter. Fig. 9

Mode	$V_{SD}\ [m/s]$	$\omega_{SD}\ [Hz]$	$V_{DLM}\ [m/s]$	$\omega_{DLM}\ [Hz]$
3	43.64	8.05	49.60	7.53
4	45.04	8.37	49.58	7.74

Table 1: Stability boundaries obtained by SD-based and DLM-based approach.

illustrates the composition of both flutter modes in terms of generalized coordinates q_i obtained by the DLM. The mode 3 is mostly dominated by an interaction of the first antisymmetric wing bending and the first antisymmetric wing torsion, whereas mode 4 mainly represents an interaction of the first symmetric wing bending and the first symmetric wing torsion (see Fig. 6). Since the natural frequencies of symmetric and antisymmetric eigenmode counterparts are very close, the behavior of both flutter mechanisms becomes akin.

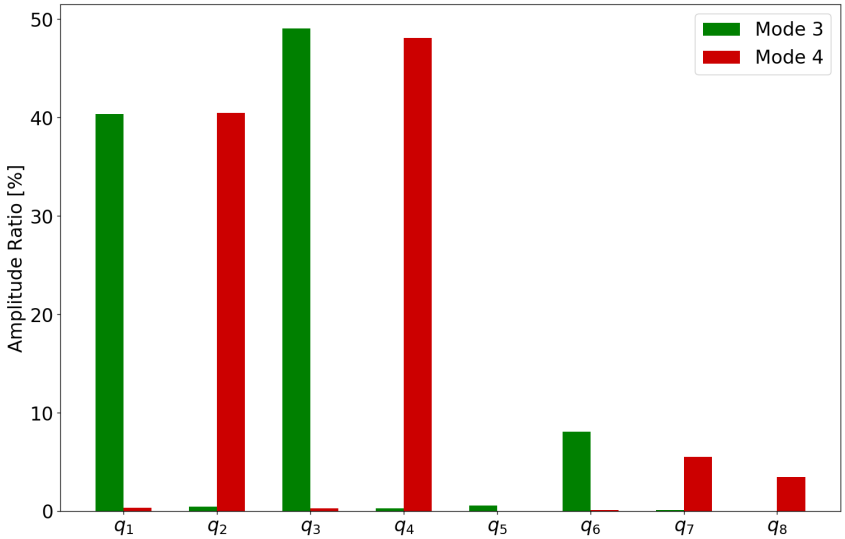

Figure 9: Ratios of each generalized coordinate q_i involved in flutter modes 3 and 4.

5 CONCLUSIONS

The goal of this work is to gain a higher confidence in the aeroelastic behavior of the FLEXOP demonstrator UAV being in development. Therefore, aerodynamic modeling for the aeroelastic analysis is provided by two different approaches, namely, the DLM of MSC.Nastran, and a SD-CFD-method. In this paper, the preliminary structural model of the UAV is introduced and the general SD-based methodology for flutter prediction is outlined. The flutter equation for the presented aeroelastic system is solved by means of the p-k method. Damping and frequency trends of the presented system show a good agreement across the two different aerodynamic models. Nevertheless, the SD-based flutter results are more conservative with respect to the predicted stability boundaries. This subject will be a matter of further study. Moreover, inclusion of rigid body modes as well as higher-order elastic modes participating in the flutter mechanism will be within the scope of future work.

6 ACKNOWLEDGEMENT

The research leading to these results is part of the FLEXOP project. This project has received funding from the European Unions Horizon 2020 research and innovation programme under grant agreement No 636307.

7 REFERENCES

[1] Wright, Jan Robert and Cooper, Jonathan Edward (2007). *Introduction to Aircraft Aeroelasticity and Loads*. John Wiley & Sons.

[2] Kreiselmaier, Erich and Laschka, Boris (2000). Small Disturbance Euler Equations: Efficient and Accurate Tool for Unsteady Load Prediction. *Journal of Aircraft*, 37(5), 770–778.

[3] Weishäupl, Caroline and Laschka, Boris (2004). Small Disturbance Euler Simulations for Delta Wing Unsteady Flows due to Harmonic Oscillations. *Journal of Aircraft*, 41(4), 782–789.

[4] Pechloff, Alexander and Laschka, Boris (2010). Small Disturbance Navier-Stokes Computations for Low-Aspect-Ratio Wing Pitching Oscillations. *Journal of Aircraft*, 47(3), 737–753.

[5] Fleischer, Dietmar and Breitsamter, Christian (2013). Efficient Computation of Unsteady Aerodynamic Loads Using Computational-Fluid-Dynamics Linearized Methods. *Journal of Aircraft*, 50(2), 425–440.

[6] Vidy, Cyrille and Katzenmeier, Lukas and Winter, Maximilian and Breitsamter, Christian (2015). Verification of the Use of Small-Disturbance CFD Aerodynamics in Flutter and Gust Analyses for Simple to Highly Complex Configurations. In *17th International Forum on Aeroelasticity and Structural Dynamics, Saint Petersburg, Russia, June 2015, pp. 1–25, Paper IFASD 2015-066*.

[7] Förster, Mark and Breitsamter, Christian (2015). Aeroelastic Prediction of Discrete Gust Loads Using Nonlinear and Time-Linearized CFD-Methods. *Journal of Aeroelasticity and Structural Dynamics*, 3(3).

[8] Winter, Maximilian and Breitsamter, Christian (2016). Neurofuzzy-Model-Based Unsteady Aerodynamic Computations Across Varying Freestream Conditions. *AIAA Journal*, 2705–2720.

[9] Maximilian Winter and Florian M. Heckmeier and Christian Breitsamter (2017). CFD-based Aeroelastic Reduced-Order Modeling Robust to Structural Parameter Variations. *Aerospace Science and Technology*, 67, 13 – 30. ISSN 1270-9638. doi: https://doi.org/10.1016/j.ast.2017.03.030.

[10] Roe, Philip L (1981). Approximate Riemann Solvers, Parameter Vectors, and Difference Schemes. *Journal of Computational Physics*, 43(2), 357–372.

[11] LeVeque, Randall J (2002). *Finite Volume Methods for Hyperbolic Problems*. Cambridge University Press.

[12] Blazek, Jiri (1994). A Multigrid LU-SSOR Scheme for the Solution of Hypersonic Flow Problems. In *32nd Aerospace Sciences Meeting and Exhibit*. p. 62.

[13] Rodden, William P and Johnson, Erwin H (2004). *MSC/NASTRAN Aeroelastic Analysis: User's Guide; Version 68*. MacNeal-Schwendler Corporation.

[14] Albano, Edward and Rodden, William P (1969). A Doublet-Lattice Method for Calculating Lift Distributions on Oscillating Surfaces in Subsonic Flows. *AIAA Journal*, 7(2), 279–285.

[15] Giesing, J and Kalman, T (1971). Subsonic Unsteady Aerodynamics for General Configurations. In *10th Aerospace Sciences Meeting*. p. 26.

[16] Duchon, Jean (1977). Splines Minimizing Rotation-Invariant Semi-Norms in Sobolev Spaces. In *Constructive Theory of Functions of Several Variables: Proceedings of a Conference Held at Oberwolfach April 25 – May 1, 1976*. Berlin, Heidelberg: Springer Berlin Heidelberg. ISBN 978-3-540-37496-1, pp. 85–100. doi:10.1007/BFb0086566.

[17] Gordon, William J and Hall, Charles A (1973). Construction of Curvilinear Co-ordinate Systems and Applications to Mesh Generation. *International Journal for Numerical Methods in Engineering*, 7(4), 461–477.

[18] Hassig, Hermann J (1971). An Approximate True Damping Solution of the Flutter Equation by Determinant Iteration. *Journal of Aircraft*, 8(11), 885–889.

COPYRIGHT STATEMENT